A crystal plasticity model based on transition state theory

CrossMark

H. Wang [a, *], L. Capolungo [b], B. Clausen [a], C.N. Tomé [a, **]

[a] Materials Science and Technology, Los Alamos National Laboratory, Los Alamos, NM, 87544, USA
[b] George Woodruff School of Mechanical Engineering, Georgia Institute of Technology, GA, 30332, USA

A R T I C L E   I N F O

A B S T R A C T

A crystal plasticity model is developed whereby explicit connections with transition state theory and with the statistics of dislocation arrangements are simultaneously enforced. Leveraging theoretical work on diffraction line profile analysis, the model predicts the distribution of internal stress (or lattice strain) resulting from that of dislocations arrangements. In turn the internal stress distribution is used to predict the activation rate of dislocation unpinning while providing an explicit connection with experimental diffraction line broadening profiles. The newly developed model is implemented into an elastic viscoplastic self-consistent (EVPSC) framework and applied to the case of stainless steel. To clearly demonstrate the additional predictive capabilities of the model, the latter is used to predict the rate sensitivity, stress and strain relaxation, Bauschinger effect, temperature effects, and evolution of the mean and the standard deviation of the lattice strains. It is found that a single set of parameters provides good agreement between the predictions and the corresponding experiments.

© 2016 Elsevier Ltd. All rights reserved.

1. Introduction

Plasticity in crystalline metals is mediated by the activation of concurrent deformation modes, each with distinct associated unit-processes, such that the mechanical response is the manifestation of the collective effects of unit process selection, activation and deactivation driven by the spatially and time evolving stress state. The combination of novel materials systems with complex microstructures (e.g. non cubic crystal structures, multiple phases, etc.) with the demands for complex forming operations (e.g, cyclic loading, biaxial loading, etc.) commands for the simultaneous predictions of the mechanical response and internal state of crystalline media during loading (e.g., texture, dislocation density, elastic strain distributions, etc.). Interestingly, a large body of long standing challenges (e.g., prediction of material instabilities, phase nucleation, damage nucleation) can be related to the limitation in predicting in a statistically representative fashion the location and values of the tails of the stress distributions involved.

Early constitutive relationships regard the aggregate as the material point and empirically reproduce experimental data by connecting an effective stress with an effective strain state of the polycrystal (Voce, 1948; Drucker and Prager, 1952). However, it was rapidly acknowledged that achieving predictive capabilities demands us to introduce physics based phenomenological constitutive relationships combined with analytical, semi-analytical or numerical homogenization methods that further increase the resolution scale at which the material point is described (e.g., the grain, a subgrain, etc.).

* Corresponding author. Tel.: +1 505 664 0321.
** Corresponding author. Tel.: +1 505 665 0892.
E-mail addresses: huamiaow@hotmail.com (H. Wang), tome@lanl.gov (C.N. Tomé).

Two parallel fields of developments have thus emerged. On the one hand, constitutive relationships were developed at the single crystal and sub single crystal scales to address predictions of creep rates, texture change, strain hardening, strain rate sensitivity, kinematic hardening, etc. in diverse material systems such as fcc, hcp, orthorhombic (McDowell, 2008).

On the other hand, homogenization methods were introduced to predict the overall response of media composed of an assembly of single crystals. The two most common strategies are Eshelbian micromechanical approaches providing access only to the mean stress and strain within the crystal, and full field Finite Element or Fast Fourier transform methods providing local intragranular information. These strategies have been applied with success for the past 30 years and the results have been reported in numerous papers, of which a few representative recent ones are (Lebensohn et al., 2008; Miller et al., 2008; Proust et al., 2009; Wang et al., 2010a; Abdolvand and Daymond, 2012; Kanjarla et al., 2012; Knezevic et al., 2015).

In all the aforementioned work, the state of the microstructure both in terms of defect arrangements and stress distribution is necessarily predicted/described with a resolution equal to that of the material point size (e.g. a grain in mean-field Eshelbian micromechanics, a voxel or element in full-field methods). As a result, elastic interactions between dislocations (both short and long range) and their associated contributions to the free energy of the system are necessarily overlooked in constitutive models. This essentially amounts to assuming that both free energy and dissipative potentials can be homogenized with same resolution. The criticality of these assumptions was largely discussed in McDowell (1995) in which the concept of statistical averaging of dissipative potentials was introduced.

The importance of the stress field resulting from dislocation interactions can also be seen from another viewpoint. Diffraction line profile analysis used to measure the elastic strain distribution projected on specific planes has largely shown that grain size, the presence of stacking faults, and more importantly the density and arrangement of dislocations in the microstructure lead to a broadening of these distributions (Balogh et al., 2006; Ungár et al. 2001, 2010). Note that the peak provides information on stresses projected along a diffraction vector, and the tails of diffraction peaks are thus representative of stress concentrations within the system. Within the material point the presence of high tensile and compressive stresses necessarily drive (or at least play a key role) in the activation and selection of dissipative processes (twin nucleation, dislocation rearrangements, and crack nucleation).

A relatively limited number of distinct statistical approaches have been proposed to circumvent these limitations. Dislocation interactions were fully introduced by Groma and Bakó (1998), Groma et al. (2003) and Csikor and Groma (2004) to analyze stress distributions of 2D straight and parallel dislocation configurations and obtain statistical properties of 2D dislocation ensembles. These authors used correlation functions to formally describe the geometrical arrangement of line defects, the evolution of dislocation density on specific slip system, and the distribution of resolved shear on the glide plane. In other works a distribution of intergranular stresses was introduced thereby leading to a distribution of critical stresses for slip activation (Li et al., 2012).

Alternatively, and at the cost of generality of the approach, rather than describing the statistics of dislocation arrangements, focus has been placed in distinguishing dislocation types according to the effect/phenomenon to be described. For example in strain gradient plasticity models and in general higher order continuum approaches the idea put forth is to distinguish dislocation populations and ascribe a back stress to the presence of polar dislocations (Cheong et al., 2005). Physically, the latter should be connected to the elastic strain field on a given side of a distributed elastic strain projected on a specific slip system.

In what follows, building on a recent publication by the authors (Wang et al., 2016a) a new constitutive model is proposed to describe the elasto-viscoplastic deformation of polycrystals subjected to complex loading histories. The model finds its roots in dislocation theory, notably to describe both evolutions of dislocation densities and the effect of their interactions on hardening, but also utilizes the transition state theory framework (Vineyard, 1957; Kocks et al., 1975) in a fashion similar to that proposed by (Busso, 1990; Monnet et al., 2013) in order to obtain estimates for the activation of slip events. Finally, and using fundamental contributions from diffraction line profile analysis (Wilkens, 1970; Groma et al., 2003), a connection between the dislocation densities and internal elastic strain distributions is developed.

More specifically, use is made of the connection between dislocation densities on different slip systems and the projected elastic strain distributions on crystallographic planes. With this extraneous information at the (sub)material point scale, a simple statistical averaging procedure is introduced by using harmonic transition state theory to predict the rate of activation for dislocation slip. The statistical mechanics based model is implemented into the elastic viscoplastic self-consistent (EVPSC) framework (Wang et al., 2010a, 2010b) and applied to the case of stainless steel. It is shown that both the connection with statistical mechanics and with the statistics of elastic strain distributions allow for the prediction of stress and strain relaxation, temperature and rate sensitivity effects, Bauschinger effect and internal strain evolution.

2. Bridging crystal plasticity constitutive models with the statistics of dislocation arrangements

2.1. A single crystal constitutive law statistically averaging the transition states

The elasto-plastic polycrystal model EVPSC used here as a platform for implementing the single crystal constitutive law is described in detail in the original publication (Wang et al., 2010a) and also in previous publications where an empirical single crystal model was proposed for interpreting the interrupted experiments (Wang et al., 2012, 2013a). We refer the reader to those works for details of the model. For the purpose of this Section let us recall that EVPSC is a finite strain formulation and the constitutive equation at a material point is expressed using an Eulerian framework as follows:

$$\dot{\bar{\sigma}} = \boldsymbol{C} : (\dot{\boldsymbol{\varepsilon}} - \dot{\boldsymbol{\varepsilon}}^p) \tag{1}$$

where $\dot{\bar{\sigma}}$ is the objective Jaumann rate of Cauchy stress $\boldsymbol{\sigma}$, $\boldsymbol{C}$ is the elastic stiffness, $\boldsymbol{\varepsilon}$ and $\boldsymbol{\varepsilon}^p$ are the total strain and plastic strain, respectively. The total strain rate at a material point is expressed as the sum of elastic and plastic contributions, with respective superscript e and p, and the total strain rate can be linearized as:

$$\dot{\varepsilon}_{ij} = \dot{\varepsilon}_{ij}^e + \dot{\varepsilon}_{ij}^p = M_{ijkl}^e \dot{\sigma}_{kl} + M_{ijkl}^p \sigma_{kl} + \dot{\varepsilon}_{ij}^0 \tag{2a}$$

with

$$\dot{\varepsilon}_{ij}^0 = \dot{\varepsilon}_{ij}^p - M_{ijkl}^p \sigma_{kl} \tag{2b}$$

In the above, M_{ijkl}^p is the viscoplastic compliance. Explicit expressions are derived in Appendix A. Adopting a crystal plasticity framework, the plastic strain rate at a material point is written as the sum of the shear rates on all slip systems ($\boldsymbol{b}^s$, $\boldsymbol{n}^s$):

$$\dot{\varepsilon}_{ij}^p = \sum_{s=1}^{N^{sys}} \overline{\dot{\gamma}^s} m_{ij}^s \tag{3}$$

where $m_{ij}^s = (b_i^s n_j^s + b_j^s n_i^s)/2$ is the Schmid tensor. $\overline{\dot{\gamma}^s}$ denotes the strain rate on system s at a given material point.

Plasticity and microstructure evolution will result from the processes of dislocation unpinning and transport, which depend on the local stress state resolved within the activation volumes of said process. Yet, the scale at which the constitutive law operates is that of the material point (i.e. much larger than the activation volume for each event to be activated). As a result, knowledge of the stress state within the material point is not sufficient to render the fact that in subzones of the material point, the stress state could be such that dislocations will be immobile, while in others dislocations could be subjected to a higher stress state (i.e. the tail of the stress distribution), for athermal and correlated obstacle bypass (Picu, 2002).

The approach followed here decomposes the material point into sub-points each with different volumes and different stresses (Fig. 1). In each sub-point, the stress state is assumed homogeneous. The overall stress distribution in a given material point reproduces the stress fluctuations due to collective interactions between dislocation segments and must have a first moment equal to the stress state at the material point. If one denotes τ^s the resolved shear stress within a given submaterial point and $\overline{\tau}^s$ the average resolved shear stress in the material point (i.e. the assembly of sub-material points), the effective shear rate can be given by an integral over the product of the shear strain rate within a sub-material point multiplying the
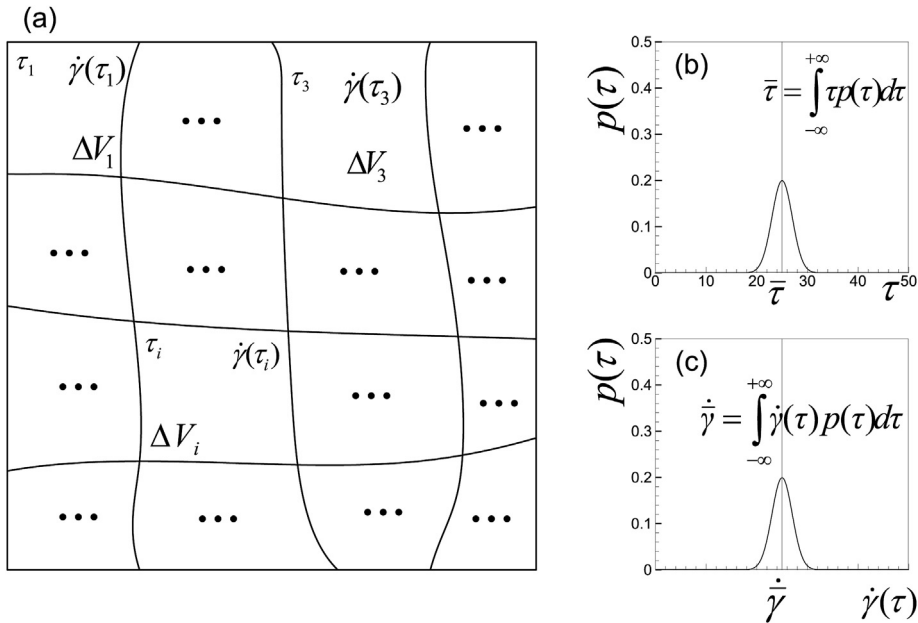

Fig. 1. Schematic representation of the distribution of the stress in a material point: a) stresses are different from a sub-material point to another; b) probabilistic distribution function for stress; and c) probabilistic distribution function for shear rate.

volume fraction it occupies. This fraction is directly given by the probability distribution function, p, of the resolved shear stress. With this, one has:

$$\overline{\dot{\gamma}^s} = \int_{-\infty}^{\infty} \dot{\gamma}(\tau^s) p(\tau^s - \overline{\tau}^s) d\tau \tag{4}$$

Using kinematic arguments, the shear rate resulting from slip on system s within a sub-material point is given by:

$$\dot{\gamma}^s = \rho^s b^s v^s \tag{5}$$

where ρ^s is the corresponding dislocation density on the system, and v^s the mean dislocation velocity on that specific system in the sub-material point. Interestingly here no distinction is made between mobile and immobile dislocations. However, the mean velocity on the system weighs in the effects of dislocations that are effectively not moving and, as a consequence, will reduce the mean dislocation velocity on the system.

Estimates of the mean dislocation velocity can be obtained by using a statistical mechanics rooted approach, very much inspired by the concept of percolation extensively discussed by Kocks et al. (1975). From this viewpoint, the mean velocity on a system is expressed as the ratio of the mean distance traveled by a dislocation upon unpinning divided by the total time for the process to occur. Here both travel and waiting times for the barrier to be overcome – with or without the assistance of thermal activation – are simultaneously accounted for. Therefore, one has:

$$v^s = \frac{L^s}{t_w^s + t_t^s} \tag{6}$$

where L^s, t_w^s and t_t^s are the mean spacing between segments, waiting time for the dislocation to de-pin and the travel time required to travel over the mean free path. In connection with the principle of similitude (Kuhlmann-Wilsdorf and Wilsdorf, 1953) and with simulations of the evolution of dislocation mean free path as a result of collective segment interactions performed by discrete dislocation dynamics simulations (Devincre et al., 2008), the mean spacing between segments can be related to the inverse of the square root of the dislocation density as follows:

$$L^s = \frac{1}{\sqrt{\alpha^{ss'} \rho^{s'}}} \tag{7}$$

where $\alpha^{ss'}$ are the latent hardening coefficients, which can be determined from discrete dislocation dynamics (DDD) simulations (Madec et al., 2002; Monnet et al., 2004; Queyreau et al., 2009; Bertin et al., 2014). L^s is not the average spacing between dislocations but the average distance traveled by dislocations before they are stored. The dependence of L^s (Eq (7)) with the latent hardening coefficients is meant to account for the fact that dislocations that do not interact strongly will be able to cut across each other easily before getting stored. Note that in the literature it has also been proposed to distinguish between latent hardening and latent storage effects (Bertin et al., 2014). This subtlety is not invoked here. The travel velocity of dislocations is fast and on the order of speed of sound (c_v) (Hirth and Lothe, 1982). The time t_t^s, for the dislocation segment to travel over the distance L^s determines the maximum shear rate that can be reached ($\dot{\gamma}^s = \rho^s b^s c_v$). It can be estimated by:

$$t_t^s = \frac{L^s}{c_v} = \frac{1}{c_v \sqrt{\alpha^{ss'} \rho^{s'}}} \tag{8}$$

The waiting time for dislocations to unpin is affected by the statistics of both, dislocation arrangement and thermal fluctuations. The latter drives the strain rate sensitivity of the system. Here the approach chosen is to rely on harmonic transition state theory as a mean to quantify such estimate (Granato and Lücke, 1956). Within this framework, the time for each event to be activated is simply written as the product of an attempt frequency and the probability for the activation barrier to be overcome as a result of both local stresses and thermal fluctuations. The former introduces the contributions of entropic changes within the system and the latter accounts for enthalpy changes within the system. The shear strain rate within each of the sub-material points is then obtained by multiplying the attempt frequency by the probability of success of the event type considered (i.e. slip on system s) at fixed stress. The probability for a dislocation segments to de-pin at a temperature T when $|\tau^s| < \tau_c^s$ is expressed as (Kocks et al., 1975),

$$Q(\tau^s) = \exp\left(-\frac{\Delta G_0}{kT}\left(1 - \left(\frac{|\tau^s|}{\tau_c^s}\right)^p\right)^q\right) \tag{9}$$

ΔG_0 denotes the effective activation energy within the sub-material point. It must be representative of many-body interactions and must account for both, athermal events (i.e. with very large activation barrier; typically $\geq$2eV), and events with particularly low activation barrier. p and q are parameters bound within [0,1] and [1,2] respectively (Kocks et al., 1975). Their

values determine the width of the probability distribution function in terms of resolved stress on system s, and of the athermal activation regime. p and q are also connected to the geometrical arrangements of obstacles. For example, for a periodic array of defects Kocks et al. (1975) estimated that p = 1/2 and q = 2. τ_c^s denotes the critical resolved shear stress within the given submaterial point; i.e. the stress threshold past which thermal activation is not required for the event to be activated. In such case, $Q(\tau^s) = 1$.

Critical resolved effective activation barrier, shear stresses on system s, attempt frequencies and dislocation mean free path (see Eq. (7)) depend on the statistical arrangement of dislocations and, more explicitly, on the length distribution of pinned segments. Rigorously, the stress state within each sub-material point —which necessarily accounts for the effect of dislocation interactions-, also depends on the density and geometrical arrangement of these dissociations (Wilkens, 1970; Ungár et al., 1999). Here for the sake of simplicity, such refinement is not taken into account and in each sub-material point the length of pinned segment and segment density is assumed uniform and therefore equal to that at the material point scale. Although this assumption sets a limit resolution for microstructure description, the motivation stems from the limited gain in predictive capabilities one would reach by considered a more complex approach. With these assumptions, the critical resolved shear stress on a given system s and in a given sub-material point is equal to that at the material point scale and given accordingly to the work of Franciosi and Zaoui (1982a, b):

$$\tau_c^s = \tau_0 + \mu^s b^s \sqrt{\alpha^{ss'} \rho^{s'}} \tag{10}$$

where μ^s, b^s are shear modulus, Burgers vector and the hardening coefficients, respectively. The shear modulus of system s is the projection of the elastic stiffness onto the system: $\mu^s = b_i^s n_j^s b_k^s n_l^s C_{ijkl}$ (C_{ijkl} is the elastic stiffness of the crystal). Notice that the mean stress in the material point, $\overline{\tau}^s$, and the threshold resolved shear stress on system s, τ_c^s, do not necessarily coincide and, furthermore, their separation can evolve with strain.

Using a statistical mechanics based reasoning applied to the case of a vibrating string, formally representing the dislocation line, Granato et al. (1958) addressed the question of entropic factors and more generally of the effective attempt frequency f_{att}^s for thermally assisted dislocation unpinning. The authors showed that f_{att}^s can be written as the product between an attack frequency (mode 1) and an entropic factor related to the ratio of the products of the natural frequencies in both the relaxed and activated states. The authors proceed with distinguishing cases of weak, intermediate and 'infinitely strong' obstacles. For the latter it is found that the attempt frequency essentially corresponds to the Debye Frequency. However, in the cases treated here, the obstacles are to be considered either weak or of intermediate strength. Indeed a material point and a sub-material point will contain a complex geometry of dislocations (i.e. in contact or not with each other) and thermally activated bypass will occur both in the cases of dislocations in contact with one another – leading to either weakly interacting cross states or to stronger interactions in the form of junctions – and at a distance from one another. In all cases, the attack frequency is the same and solely the entropic factor changes. Therefore, one can express the effective attempt frequency as follows:

$$f_{att}^s = \varsigma \nu_1 \tag{11}$$

ς denotes the entropy factor, in the order of ~1, and ν_1 refers to the attack frequency. The latter is given as the ratio of the speed of sound by the length of pinned vibrating segments (given here by Eq. (8)). Therefore one has (Granato et al., 1964):

$$\nu_1 = c_\nu \sqrt{\alpha^{ss'} \rho^{s'}} \tag{12}$$

It is to be noted here that the effective attempt frequency will therefore be several orders of magnitude lower than the Debye frequency. With this, the waiting time t_w^s is:

$$t_w^s = \frac{1}{f_{att}^s Q(\tau^s)} = \frac{1}{c_\nu \sqrt{\alpha^{ss'} \rho^{s'}} Q(\tau^s)} \tag{13}$$

when $|\tau^s| < \tau_c^s$, the travel time can be ignored because the waiting time calculated from Eq. (6) is much larger than the travel time. For $|\tau^s| \geq \tau_c^s$, the dislocation segment de-pins instantaneously ($t_w^s = 0$). Therefore, the shear rate on a slip system within a submaterial point can be expressed as:

$$\dot{\gamma}^s = \begin{cases} \rho^s b^s c_\nu \exp\left(-\frac{\Delta G_0}{kT}\left(1 - \left(\frac{|\tau^s|}{\tau_c^s}\right)^p\right)^q\right) sign(\tau^s) & |\tau^s| < \tau_c^s \\ \rho^s b^s c_\nu sign(\tau^s) & |\tau^s| \geq \tau_c^s \end{cases} \tag{14}$$

Fig. 2 illustrates the shear rate as a function of the resolved shear stress for $p = 2/3$, $q = 3/2$ and for $p = 1/2$, $q = 2$. As can be seen, the shear rate becomes relevant when the resolved shear stress approaches the threshold resistance τ_c. The parameters p and $q = 1/p$ affect the predicted results significantly: higher p will give smaller shear rates. The shear rates given by the conventional power law are also included for comparison purposes ($\dot{\gamma} = (\tau/\tau_c)^n$, red lines in Fig. 2), and show that the
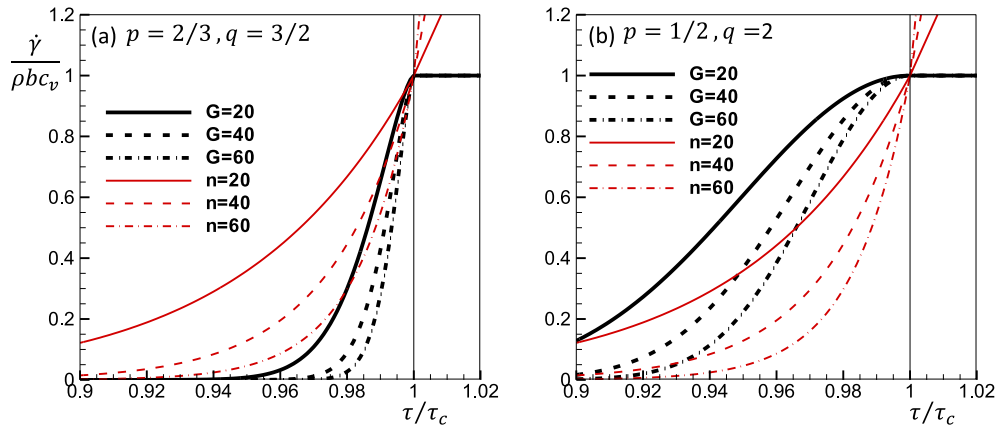
Fig. 2. Schematic representation of the shear rate and shear stress relation: (a) p = 2/3, q = 3/2, and (b) p = 1/2, q = 2. The shear rates calculated from the conventional power law $\dot{\gamma} = (\tau/\tau_c)^n$ are also included for comparison purposes.

conventional power law can be an alternative to calculate the shear rate. In a recent constitutive model that relies on the use of harmonic transition state theory to quantify the shear strain rate on specific slip systems, Monnet et al. (2013) estimated the dislocation velocity at low temperature as resulting from the product of a frequency factor and a probability of successful activation. While the philosophy applied is similar to ours, the specific features and assumptions are different. Monnet et al. assume a constant frequency factor and constant mobile dislocation density while current work does not rely on these assumptions.

Slip necessarily leads to a change in both the arrangement and densities of dislocations. The dislocation density ρ^s is assumed equal in all submaterial points and its evolution is given by the balance between a storage and a recovery term.

$$\frac{d\rho^s}{d\gamma^s} = k_1 \sqrt{\rho^s} - k_2 \rho^s \tag{15}$$

Rigorously, equation (15) and particularly its first term, formally describing the rate of dislocation storage should depend on the latent storage effects resulting from the presence of dislocation on distinct slip systems. This approach was actually followed in a series of work (Bertin et al., 2014; Devincre et al., 2008). Here for the sake of simplicity, and because the model is applied to a simple face center cubic system in the case of relatively simple loading conditions such contributions are neglected.

Following the approach proposed by (Beyerlein and Tomé, 2008) dislocation recovery is given by:

$$k_2 = \frac{\chi b^s}{g^s} \left(1 - \frac{kT}{D^s (b^s)^3} \log\left(\frac{|\dot{\varepsilon}|}{\dot{\varepsilon}_0}\right) \right) \tag{16}$$

$g^s, D^s, \dot{\varepsilon} = \sqrt{\frac{2}{3}\dot{\varepsilon}_{ij}\dot{\varepsilon}_{ij}}, \dot{\varepsilon}_0, \chi$ denote the activation barrier for recovery processes, a drag stress, Von-Mises equivalent strain rate, reference strain rate, and a fitting parameter, respectively.

2.2. Stress state distribution within a material point: connections with line profile analysis

As stated above, the shear strain rate is computed in a series of submaterial points each with their own stress state. Note that the distinction between the average stress at a material point and a lower scale stress (or micro-force) is the key motivation of micro-morphic approaches (Gurtin, 2000; Forest, 2009). In the approach proposed, the probability distribution function of the stress state within the material point is not necessarily symmetrical about its mean. Here the macro-homogeneity condition is assumed that the mean of the internal stresses is equal to the homogeneous stress in the crystal given by the effective medium model assumptions.

Numerous experiments and models of diffraction line broadening show that, in the absence of large contrast in the dislocation distribution within the coherently diffracting domain, diffraction line profiles can accurately be fitted with Gaussian distributions. When such condition is not met, then the diffraction peak is not necessarily symmetric and it was suggested that exponentially modified Gaussian distribution provide a better fit to experimental data (Groma et al., 1988). For the sake of simplicity, a Gaussian distribution explicitly described by its variance and its mean is used here to describe each component of the elastic strain tensor.

In what follows we provide a comprehensive derivation of the connections between internal elastic strains, crystallographic peak broadening, and distribution of resolved shears in crystallographic planes. The statistical definitions and relations being used can be found in Appendix B. In addition, 2nd and 4th order symmetric tensors are expressed as 6×1 and 6×6 matrices using a b-basis of symmetric 2nd order tensors. To avoid misunderstandings, the summations over the index λ will be written explicitly. Such representation is also defined in Appendix B, and allows us to avoid algebraic redundancies associated with the Cartesian components of symmetric tensors.

The projection $\varepsilon^{(k)}$ of the elastic strain along a direction $\boldsymbol{n}^{(k)}$ perpendicular to a diffracting plane k is:

$$\varepsilon^{(k)} = n_i^{(k)} n_j^{(k)} \varepsilon_{ij}^{el} = \frac{1}{2} \left(n_i^{(k)} n_j^{(k)} + n_j^{(k)} n_i^{(k)} \right) \varepsilon_{ij}^{el} = N_{ij}^{(k)} \varepsilon_{ij}^{el} = \sum_\lambda N^{(k)\lambda} \varepsilon^\lambda \tag{17}$$

In pioneering work in the area of line profile analysis, Wilkens (1970) considered the problem of diffraction line broadening resulting from the presence of restrictedly randomly distributed dislocations within a diffracting domain. The author showed that if the only contributions of first gradients in the displacement fields are considered, i.e. under the assumption of Warren and Averbach (1950), the mean square projected strain can be expressed as a function of the dislocation density. The result was later extended to the case of crystals containing dislocations on several slip systems and of different character (i.e. edge and screw). This variance $var(\varepsilon^{(k)})$ can be written as a contribution from all the dislocation systems (Wilkens, 1970; Ungár et al., 1999):

$$var\left(\varepsilon^{(k)} \right) = \sum_s \frac{\rho^s (b^s)^2}{4\pi} C^{(k)s} f(\eta^s) \tag{18}$$

The factors contributing to the mean square strain deviation are the contrast factors $C^{(k)s}$, the Wilkens function $f(\eta^s)$, the dislocation densities on each system and their respective Burgers vector. The contrast factors reflect the fact that, depending on the diffraction vector $\boldsymbol{n}^{(k)}$, a given dislocation population will contribute to a different extent to line broadening, depending on the projection of their elastic strain fields along the diffraction direction. The contrast factors are thus different for edge and for screw dislocations. In what follows we assume equal proportion of edge and screw components in every system, while the corresponding contrast factors are different for edge and screw, results are not particularly sensitive to this choice. In addition, eq. (18) shows a dependence of the mean square strain on the Wilkens function $f(\eta^s)$. The latter depends on the degree of order/organization of the dislocation structure, represented by the variable η^s. Here, to maintain a numerically tractable model, these levels of refinements are disregarded and $f(\eta^s)$ is set constant and equal to 0.5. As detailed in the work of Wilkens and later in that of Groma et al. this function typically takes values ranging from ~10 for small values of η^s (i.e. 0.1) to ~100 for large values of η^s (i.e. 1). Admittedly the value chosen here is small but within a realistic range. The specific choice of $f(\eta^s)$ affects the width of the strain distribution and therefore the rate of activation of events. Any uncertainty arising from $f(\eta^s)$ can therefore be compensated by the choice of parameters in the Arrhenius law (see eq. (14)).

Our ultimate aim is to find the standard deviation of the resolved shear stresses acting on slip systems s. Those are related to the standard deviation of the stress components, which are in turn a function of the standard deviation of the elastic strain components. As a consequence, in what follows we write the strain projected along the diffracting direction $\boldsymbol{n}^{(k)}$ (Eq. (17)) as a linear combination of the variance of the elastic strain components.[1] By solving the linear system it will be possible to obtain the latter. From a mathematical standpoint, if each component of strain can be described with a separate Gaussian distribution, any linear combination of strain components is therefore necessarily normally distributed. Denote with $var(\varepsilon^\lambda)$ and $covar(\varepsilon^\lambda, \varepsilon^{\lambda'})$ the variance associated with ε^λ and the covariance between ε^λ and $\varepsilon^{\lambda'}$. Using Eq. (17) and the properties of variance described in Appendix B the variance $var(\varepsilon^{(k)})$ of the projected strain along the diffraction vector $\boldsymbol{n}^{(k)}$ is:

$$\mathrm{var}\left(\varepsilon^{(k)} \right) = \sum_\lambda \left(N^{(k)\lambda} \right)^2 var\left(\varepsilon^\lambda \right) + \sum_{\substack{\lambda, \lambda' \\ \lambda \neq \lambda'}} N^{(k)\lambda} N^{(k)\lambda'} covar\left(\varepsilon^\lambda, \varepsilon^{\lambda'} \right) \tag{19a}$$

While both, $var(\varepsilon^\lambda)$ and $covar(\varepsilon^\lambda, \varepsilon^{\lambda'})$ are unknowns, only the values of $var(\varepsilon^\lambda)$ are required in what follows for deriving the stress dispersion. Here we assume that ε^λ and $\varepsilon^{\lambda'}$ are uncorrelated, which means that $covar(\varepsilon^\lambda, \varepsilon^{\lambda'}) = 0$ (see Appendix B), and Eq. (19a) is reduced to:

$$\mathrm{var}\left(\varepsilon^{(k)} \right) = \sum_\lambda \left(N^{(k)\lambda} \right)^2 var\left(\varepsilon^\lambda \right) \tag{19b}$$

Combining Eqs. (18) and (19) gives a symmetric linear system:

---

[1] The variance is the square of the standard deviation.

$$\sum_{\lambda} \left(N^{(k)\lambda} \right)^2 var\left(\varepsilon^\lambda \right) = \sum_s \frac{\rho^s (b^s)^2}{4\pi} C^{(k)s} f(\eta^s) \tag{20}$$

from which the 6 unknowns $var(\varepsilon^\lambda)$ can be obtained. To do so, contrast factors for edge and screw dislocations associated with 6 different diffraction vectors $\boldsymbol{n}^{(k)}$ have to be used. In this work, the six diffraction planes used are $\boldsymbol{n}^1 = \{100\}$, $\boldsymbol{n}^2 = \{010\}$, $\boldsymbol{n}^3 = \{001\}$, $\boldsymbol{n}^4 = \sqrt{2}/2\{110\}$, $\boldsymbol{n}^5 = \sqrt{2}/2\{101\}$, and $\boldsymbol{n}^6 = \sqrt{2}/2\{011\}$. We compute the 12 associated contrast factors $C^{(k)s}$ for the edge and the screw dislocation components using the software ANICZ (http://metal.elte.hu/anizc/program-cubic.html). Further, we assume that the dislocation population ρ^s is composed of equal parts edge and screw segments. In case one would not invoke the non-correlation assumption the system to be solved consists of 21 unknowns and, clearly, 21 diffraction vectors (many of them not accessible experimentally) have to be included in the computation.

Next, if one uses Hooke's law with stress, strain and elastic stiffness compliance tensors expressed in the b-basis (see Appendix B): $\sigma^\lambda = C^{\lambda\lambda'} \varepsilon^{\lambda'}$ one can calculate the variance of the stress components as:

$$var\left(\sigma^\lambda \right) = \sum_{\lambda'} var\left(C^{\lambda\lambda'} \varepsilon^{\lambda'} \right) = \sum_{\lambda'} \left(C^{\lambda\lambda'} \right)^2 var\left(\varepsilon^{\lambda'} \right) \tag{21}$$

Finally, using the form of the resolved shear stress on system s:

$$\tau^s = \frac{1}{2} \left(n_i^s b_j^s + n_j^s b_i^s \right) \sigma_{ij} = \sum_\lambda m^{s\lambda} \sigma^{s\lambda} \tag{22}$$

The variance of the resolved shear on system s is given by:

$$var(\tau^s) = \sum_\lambda \left(m^{s\lambda} \right)^2 var\left(\sigma^{s\lambda} \right) \tag{23}$$

This last result provides the variances that enter in the Gaussian probability distribution function on system s, given by:

$$p\left(\tau^s - \overline{\tau}^s \right) = \frac{1}{\sqrt{2\pi var(\tau^s)}} \exp\left(-\left(\frac{\tau^s - \overline{\tau}^s)^2}{2var(\tau^s)} \right) \right) \tag{24}$$

Note that in previous work (Wang et al., 2016a) the variance of the resolved shear stress was assumed to be the same for all slip systems and only dependent on the total dislocation density. The current approach, on the other hand, allows connecting a constitutive model, valid at the material point, to measures of diffraction line broadening, and thus provides a bridge between experiments and modeling.

The approach delineated above relies on the development of Wilkens in which mathematical assumptions were necessary in order to write Eq. (18). However, Balogh et al. (2012) showed, using discrete dislocation dynamics simulations to quantify the error resulting from these assumptions, that the Wilkens model provides predictions of the mean square strain that are within a very reasonable factor of 3 different than the numerical variances. A caveat is that the configurations tested by Balogh et al. (2012) were single populations of randomly distributed curved dislocations, and the error associated with the Wilkens model when applied to more complex configurations could be larger.

In the derivation presented above we use Eq. (18) to obtain the variance in directional strains and use it to provide a theoretical estimate of the variance in resolved shears. In what follows, we will derive a comparison approach between the theoretical variance in directional strain and the experimentally measured peak broadening. The broadening of a diffraction peak is commonly characterized by the full width at half maximum (FWHM) which is provided by the in-situ neutron diffraction measurement and is usually expressed in units of time of flight (microsecs). In a time of flight (TOF) neutron diffraction measurement, a short pulse of neutrons containing a range of wavelengths is incident on a sample. Neutrons of a given wavelength are diffracted by lattice plane $\boldsymbol{n}^{(k)}$ according to Bragg's condition. Since the kinetic energy and hence the velocity of neutrons depends on the wavelength, their time-of-flight between the source and the detector bank also depends on wavelength. For the diffracted neutron, the relationship between the $TOF^{(k)}$ in microseconds and the d-spacing of a reflection $d^{(k)}$ in angstroms is given by (Larson and Von Dreele, 2004),

$$TOF^k = A_1 \left(d^k \right)^2 + A_2 d^k + A_3 \tag{25}$$

where A_1, A_2 and A_3 are generally known as 'the diffraction constants' for the instrument. The d-spacing in terms of TOF follows from solving Eq. (25) as:

$$d^{(k)} = \frac{-A_2 + \sqrt{A_2^2 + 4A_1\left(TOF^{(k)} - A_3\right)}}{2A_1} \tag{26}$$

For a diffraction peak described by a Gaussian function the FWHM is related to the standard deviation of TOF as

$$FWHM^k = \sqrt{8ln2}\,SD\left(TOF^{(k)}\right) = \sqrt{8ln2}\sqrt{var\left(TOF^{(k)}\right)} \tag{27}$$

Applying to Eq. (26) the property of the variance of a function $(f(x)) = (f'(\overline{x}))^2 var(x)$, and using Eq. (27), the standard deviation of the d-spacing is:

$$SD\left(d^{(k)}\right) = \frac{SD\left(TOF^{(k)}\right)}{\sqrt{A_2^2 + 4A_1\left(TOF^{(k)} - A_3\right)}} = \frac{1}{\sqrt{A_2^2 + 4A_1\left(TOF^{(k)} - A_3\right)}}\frac{FWHM^k}{\sqrt{8ln2}} \tag{28}$$

Therefore the standard deviation for the peak of diffraction plane $\boldsymbol{n}^{(k)}$ in terms of internal elastic strains given by Eq. (20) is

$$SD\left(N^{(k)\lambda}\varepsilon^\lambda\right) = SD\left(\varepsilon^{(k)}\right) = SD\left(\frac{d^{(k)} - d_0^{(k)}}{d_0^{(k)}}\right) = \frac{SD\left(d^{(k)}\right)}{d_0^{(k)}} \tag{29}$$

The model predicts $SD(N^{(k)\lambda}\varepsilon^\lambda)$ and the experiment provides $\frac{SD(d^{(k)})}{d_0^{(k)}}$. As a consequence, we have the possibility of making a direct comparison between model and peak profile measurement.

3. Application to stainless steel

3.1. Materials and methods

The material used in the present work is a standard 316L austenitic stainless steel alloy. The spectrometer for high intensity pressure and preferred orientation (HIPPO) (Wenk et al., 2003) at LANSCE (the Los Alamos Neutron Science Center) was used to measure the initial texture of the tested materials. Fig. 3 shows the {111}, {200} and {220} pole figures of the initial texture used for simulation. The initial texture used in the model simulations is derived from the experimental orientation distribution function and consists of 23,328 discrete orientations, by division of Euler space into $5 \times 5 \times 5$ cells, with volume fractions assigned to represent the measured initial texture. The pole figures indicate that the as-received stainless steel has a very weak rolling texture.

In situ neutron diffraction measurements were performed during tensile deformation using the VULCAN instrument at the Spallation Neutron Source (SNS) (An et al., 2011). In order to study the effect of stress relaxation and strain creep on lattice strain development, three experiments were conducted at room temperature. The detailed description of the experiments can be found elsewhere (Wang et al., 2013a). The first is a monotonic uniaxial tension tests under strain rate of $6 \times 10^{-6}s^{-1}$. The second experiment is uniaxial tension with strain-controlled holdings during measuring times. Stress relaxation is clearly observed during holding both in the macroscopic stress–strain response and in the internal lattice strains. The third experiment is uniaxial tension with stress-controlled holdings, and creep is observed during holding time. For the tests with interrupts, the loading rate is $1 \times 10^{-4}s^{-1}$ between strain holds and the holding times are 15 min (900 s). Although as we show in Section 3.4 there is a difference in predicted flow stress between the 10^{-6} and the $10^{-4}s^{-1}$ monotonic tension tests, the flow stress in the intervals between holds is nearly indistinguishable from the one of the monotonic loading test performed at the
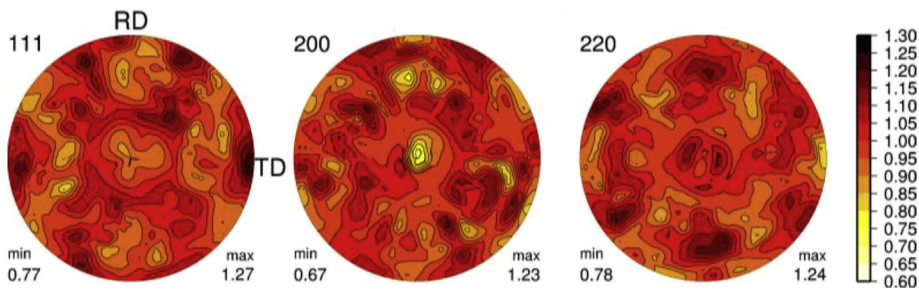

Fig. 3. {111}, {200}, {220} pole figures for the initial texture. Observe that it is nearly random.

strain rate of $6 \times 10^{-6}s^{-1}$. We attribute this coincidence to the low rate sensitivity of stainless steel at room temperature, and to the dislocation recovery taking place during holds. We find that the hardening parameters adjusted to the monotonic experiment at $6 \times 10^{-6}s^{-1}$ predict well the stress-strain reloads associated with the two interrupted experiments.

3.2. Polycrystal simulation and parameters identification

The single crystal constitutive model based on transition state theory (TST) described above is implemented into the EVPSC framework for polycrystalline materials (denoted as TST model). As said above, a complete description of the EVPSC model can be found in Wang et al. (2010a). EVPSC model has been used to study twinning and detwinning in magnesium alloys (Wang et al., 2013b, 2013c), the forming limit of magnesium alloy AZ31B rolled sheet (Wang et al., 2011, 2015a), and the torsion of magnesium alloy AZ31 extruded bar (Wu et al., 2012; Wang et al., 2015b). Recently, it has been successfully used to interpret the internal lattice strain development in stainless steels (Wang et al., 2013a; Guo et al., 2015), zirconium alloys (Qiao et al., 2015), and magnesium alloys (Lee et al., 2014).

EVPSC tensile simulations were performed at the experimental strain rate of $6 \times 10^{-6}s^{-1}$ for the monotonic load, and at $1 \times 10^{-4}s^{-1}$ for the loading between interrupts for both strain-controlled and stress-controlled tests. As shown in Fig. 4a, the fitted monotonic stress–strain curve coincides with the experimental one previously reported by Wang et al. (2013a) for the same steel for a strain rate of $6 \times 10^{-6}s^{-1}$. The parameters of the model adjusted to match the experimental stress strain curve are listed in Table 1. The authors acknowledge that the value of τ_0 used in the present paper is higher than that reported by Karaman et al. (2001) in single crystal 316L (80–90 MPa), and by (Monnet and Pouchon, 2013) in very detailed pillar compression experiments on 316L steel revealing a 95 MPa friction stress in a large single crystal. As usual, the discrepancy between the values we used here and those reported for single crystals may partly be attributed to grain boundary effects. The single crystal elastic constants used are $C_{11} = 204.6$, $C_{12} = 137.7$ and $C_{44} = 126.2$ (unit of GPa) (Clausen et al., 1999). The latent hardening coefficients used are those reported by Devincre et al. (2008), who used discrete dislocation dynamics simulations to quantify these parameters. In the case of face centered cubic systems the five types of dislocation interactions and the corresponding hardening parameters (in parenthesis) are: coplanar (0.009), collinear interaction leading to annihilation (0.55), Hirth lock (0.05), Lomer lock (0.07) and glissile junction formation (0.1).

Fig. 4a shows the experimental and simulated macroscopic stress strain curve. The predicted dislocation density (Fig. 4b) is of the order of 10^{14} m^{-2}, consistent with the experimental observations. Fig. 4c shows the standard deviations of resolved shear stress averaged over all grains with respect to each numbered slip system (1–12) as a function of the strain (dash red line). The corresponding average value over all grains and systems is also included in Fig. 4c (solid black line).

3.3. Stress and strain relaxation

Stress relaxation and strain relaxation are studied by simulating uniaxial tension with strain holding and stress holding. The boundary conditions for stress relaxation is: $\dot{\varepsilon}_{11} = 0$, $\dot{\sigma}_{ij} = 0$ except $\dot{\sigma}_{11} \neq 0$ as the tensile stress σ_{11} is the only non-zero stress component. The stress relaxation is simulated by holding the total strain constant for 900 s, following which a strain rate of $10^{-4}s^{-1}$ is applied until reaching the next holding point. The boundary condition for creep simulation is $\dot{\sigma}_{ij} = 0$ as the applied stress is held constant during creep time intervals of 900 s.

Fig. 5a and b shows the macroscopic stress strain curve with strain and stress holdings. Fig. 5c shows predicted macroscopic stress with time during strain holding. The stress drops (stress relaxation) are observed at every strain-controlled holding. During strain holding, the decrease of the average RSS shifts the RSS distribution away from CRSS and results in a longer waiting time for the dislocation segments to de-pin (i.e., a smaller shear rate). Fig. 5d shows predicted macroscopic strain with time during stress holding. The strain plateaus (creep sections) are observed at every load level. The amount of
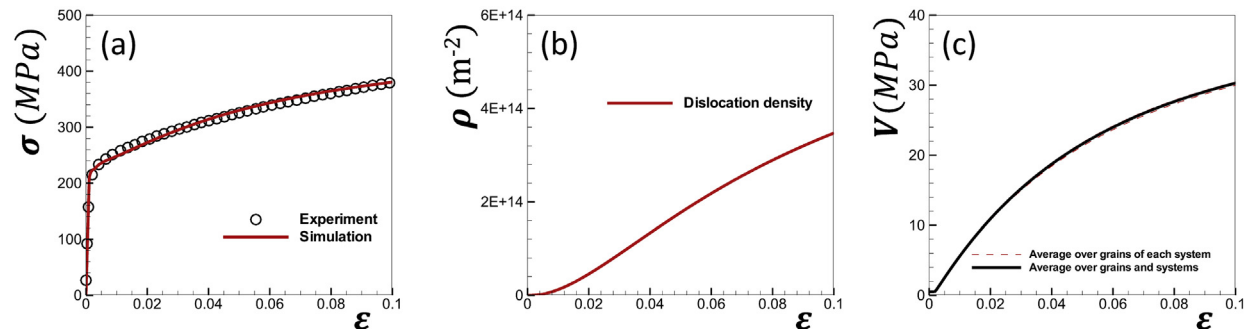

Fig. 4. (a) Experimental and simulated macroscopic stress strain curve, corresponding to tension along the RD at 298 K and 6×10^{-6}/s (Wang et al., 2013a, b); (b) predicted evolution of the total dislocation density; (c) evolution of average standard deviation in resolved shear obtained by averaging the standard deviations in all systems in all grains (solid black line) and averaging individual systems over all grains (dash red line). (For interpretation of the references to colour in this figure legend, the reader is referred to the web version of this article.)

Table 1
Constitutive model parameters used in the current study.

$K_1(1/m)$	$D(MPa)$	$\Delta G_0(eV)$	$c_v(m/s)$	p	q	χ	$\rho_0(1/m^2)$	$\tau_0(MPa)$	$T(K)$	$b(\text{Å})$
5.5×10^8	100	6	1500	2/3	3/2	0.2	1×10^7	118	298	2.546
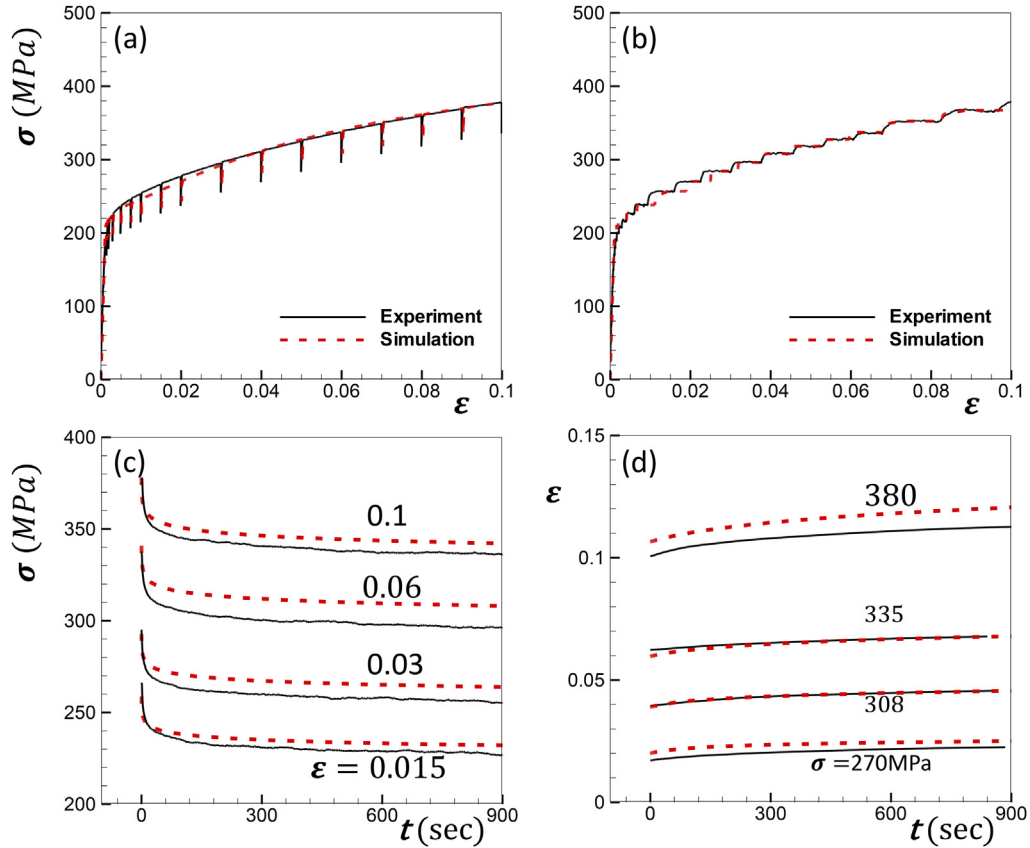
Fig. 5. Simulated stress strain curves under tension with (a) strain holding; (b) stress holding. (c) stress evolution during strain holding, plot for different holding strains; (d) strain evolution during stress holding, plot for different holding stresses.

creep deformation increases as the stress level increases. During stress holding, the increase of CRSS due to the stored dislocation shifts the CRSS away from the average RSS and also results in a longer waiting time for the dislocation segments to de-pin (i.e., a smaller shear rate). The model predicts well the amount and time dependence of the stress drop and of the creep strain.

3.4. Lattice strain and peak width predictions

The longitudinal and transverse lattice strains and their standard deviation (Eq. (29)) under monotonic tension are predicted by the model as explained in Section 2.2. Fig. 6 compares the experimental and predicted evolution of lattice strain for the {111}, {200} and {220} plane families aligned with the longitudinal and transverse scattering directions as a function of applied stress. The internal strains develop linearly with stress in the grains along the different scattering directions, up to about 170 MPa. The plastically hard oriented grains (i.e. the {200} grains in both longitudinal and transverse directions) bear more internal lattice strain and deform elastically much longer. On the contrary, the plastically soft oriented grains (i.e. {220} oriented grains in the longitudinal direction) accommodate more of the imposed strain plastically and therefore carry less internal stress (i.e. lattice strain).

As discussed in Section 2.2, if the diffraction peaks are Gaussian the standard deviation of the peak (in terms of lattice strain) can be derived from the relation with the measured FWHM using $FWHM^k = \sqrt{8 \ln(2)} SD(\varepsilon^k)$ and can be compared with the predicted standard deviation of the {hkl} peak ($SD(\varepsilon^{(k)})$ given by Eq. (19)). The latter is obtained by averaging over all the grains contributing to the {hkl} reflection. As discussed by Kanjarla et al. (2012), the standard deviation of the peaks is affected significantly by the instrument broadening. In order to remove the effect of instrument broadening, and considering that for
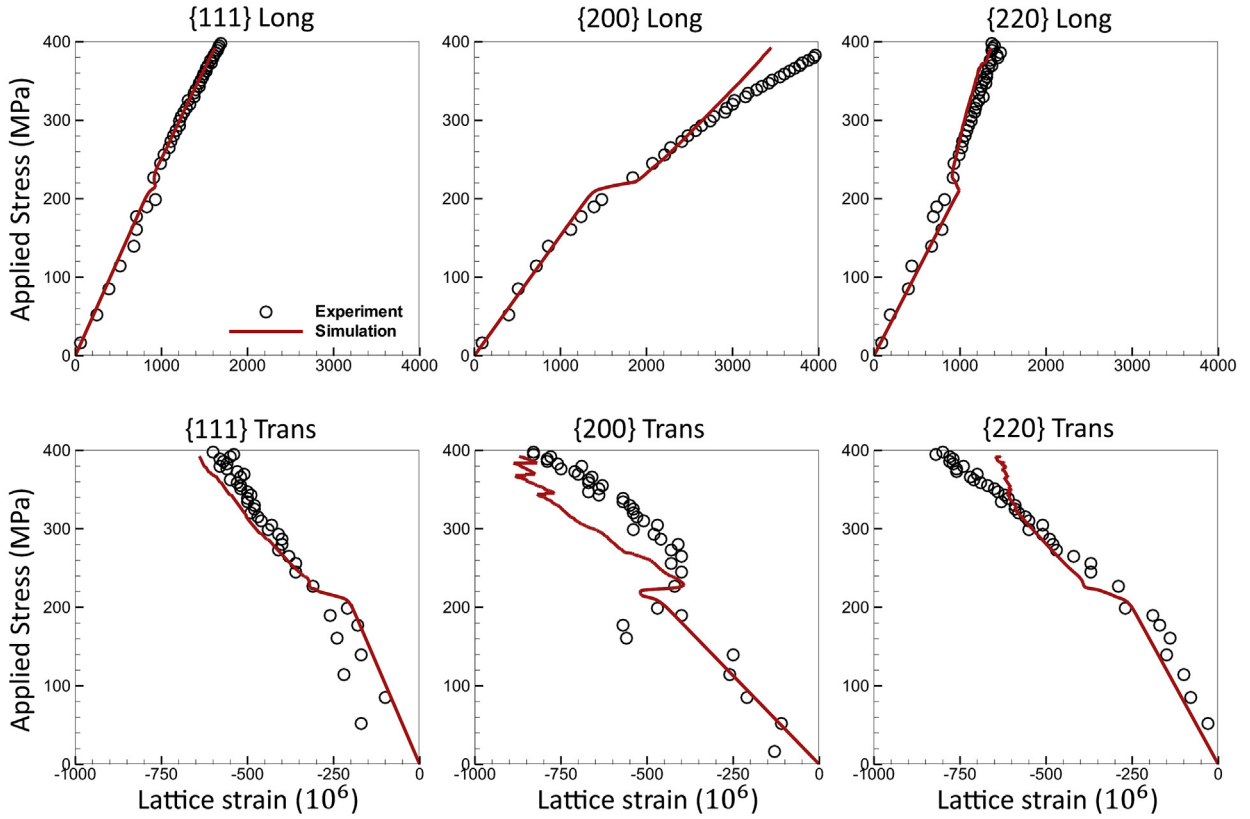
Fig. 6. Evolution of the {111}, {200} and {220} lattice strains as measured and as predicted by TST model.

an annealed material it is negligible before the yielding point, the standard deviation of peaks at yield point ($\sigma = 220\ MPa$) is used as zero reference for measured and simulated deviations. Any increase above such reference is attributed to evolution of dislocation densities. The predicted and measured standard deviations of the {111}, {200} and {220} internal elastic strains are compared in Fig. 7, and it can be seen that they are in very good agreement, indicating that the predicted evolution of dislocation density is consistent with experiment. While other factors affecting broadening, such as grain size or non-uniform lattice distortion, are not accounted for here, it is likely that they do not affect measurements in a meaningful way.

Remarkably, it is shown here that, despite the fact that a mean-field Eshelbian micromechanics polycrystal homogenization method is used, the model can successfully predict both the projected mean strain and their variance. The latter is representative of the stress field and elastic strain field resulting from dislocation interactions at a sub-material point length scale.

3.5. Perspectives: rate sensitivity, temperature effects and complex loading paths

The main motivation for the constitutive model developed here is to provide a link between line profile analysis, its connection with statistics of dislocation arrangements, and the associated internal stress distribution, using the statistical mechanics approach of transition state theory. Sections 3.3 and 3.4 clearly show the capability of the model in this regard. The present section aims at demonstrating other predictive capabilities of the approach. Due to the lack of specific experimental data for the material utilized in this work, here we will simply show how the model performs at different strain rates, different temperatures, or under loading path changes.

First, because of its connection with harmonic transition state theory, the model can reproduce both the effects of temperature and strain rate on the mechanical response of polycrystals. Simulated stress strain curves with strain rates of $1 \times 10^{-6}\ s^{-1}, 1 \times 10^{-4}\ s^{-1}, 1 \times 10^{-2}\ s^{-1}$ and $1.0\ s^{-1}$ are depicted in Fig. 8a. The rate sensitivity evidenced by these results is weak, and comparable to the one reported by Talyan et al. (1998) for a similar 316 Stainless Steel ($0.015 < m < 0.020$).

Higher strain rate induces higher flow stress and higher hardening rate. This is clearly illustrated for an individual slip system: if one shear strain rate is 3.3 times larger than the other, i.e. $\dot{\gamma}_1/\dot{\gamma}_2 = 3.3$, Eq. (15) will give $(1 - (|\tau_2^s|/\tau_{c2}^s)^{2/3})^{3/2} - (1 - (|\tau_1^s|/\tau_{c1}^s)^{2/3})^{3/2} = \ln(3.3)\frac{kT}{\Delta G_0}$. As a consequence, the value of $kT/\Delta G_0$ (=0.0043) determines the
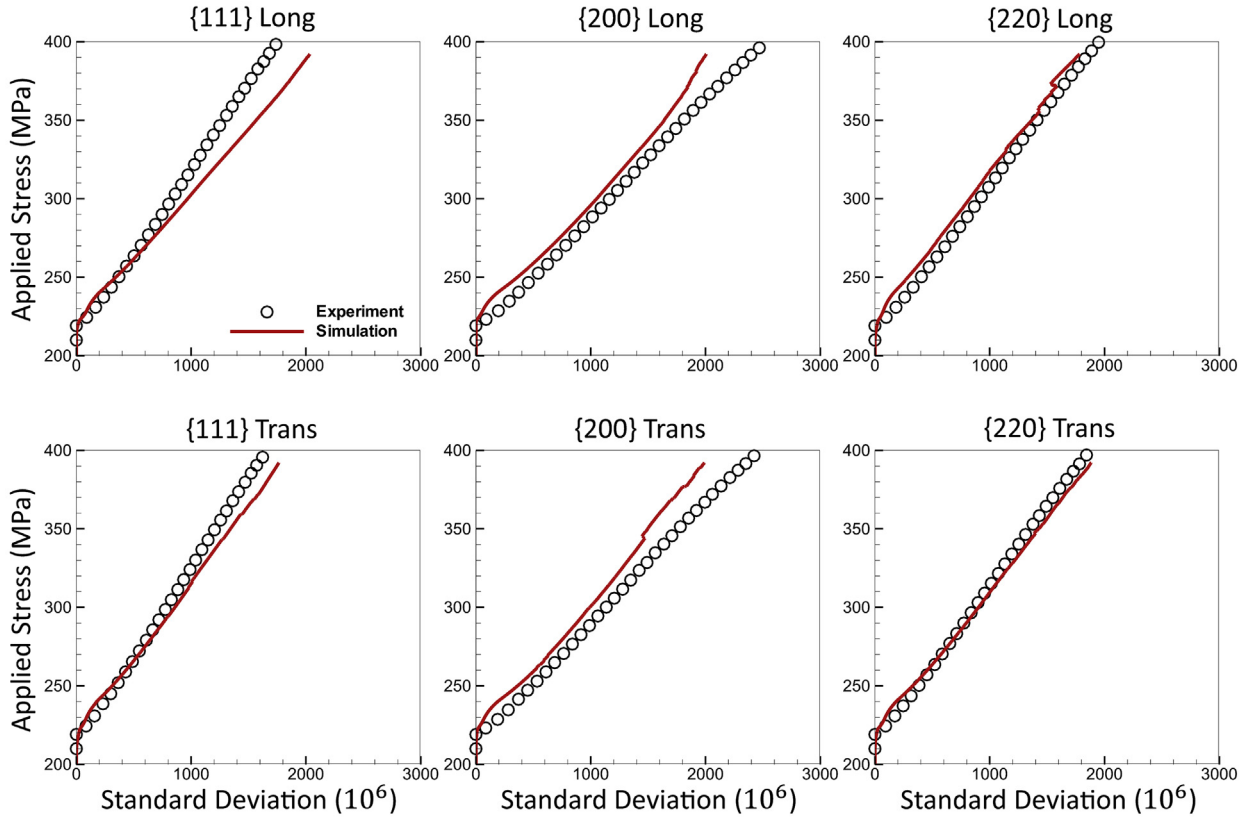
Fig. 7. Evolution of the {111}, {200} and {220} lattice strain standard deviations from measured FWHM and as predicted by TST model (Eq. (19)).
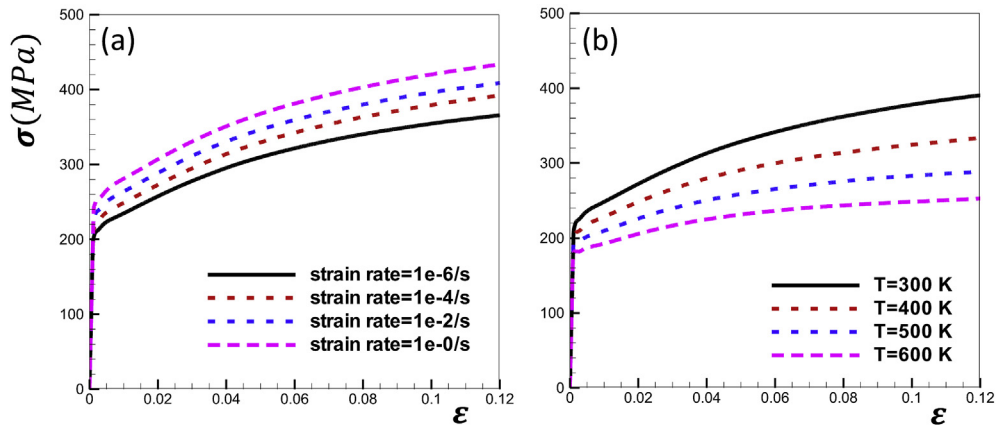

Fig. 8. Simulated stress strain response under different conditions for the 316L stainless steel used in this work. (a) monotonic tension along RD at 300 K and strain rates of $1 \times 10^{-6}\,s^{-1}$, $1 \times 10^{-4}\,s^{-1}$, $1 \times 10^{-2}\,s^{-1}$ and $1.0\,s^{-1}$; (b) monotonic tension along RD at a strain rate of $1 \times 10^{-4}\,s^{-1}$ and temperatures of 300 K, 400 K, 500 K and 600 K.

difference between the two flow stresses. Temperature T and dislocation activation energy ΔG_0 govern the rate sensitivity of the material, which is higher at higher temperature or lower activation energy.

Next, the effect of temperature is studied by simulating the response of our stainless steel under tension at temperatures of 300 K, 400 K, 500 K and 600 K (Fig. 8b). The effect of temperature on the mechanical behavior, namely, a decrease in the flow stress with temperature increase is correctly captured by the TST model. The drop in flow stress with temperature is of the same order as the one experimental one reported by Wang et al. (2016b) for TRIP steels.
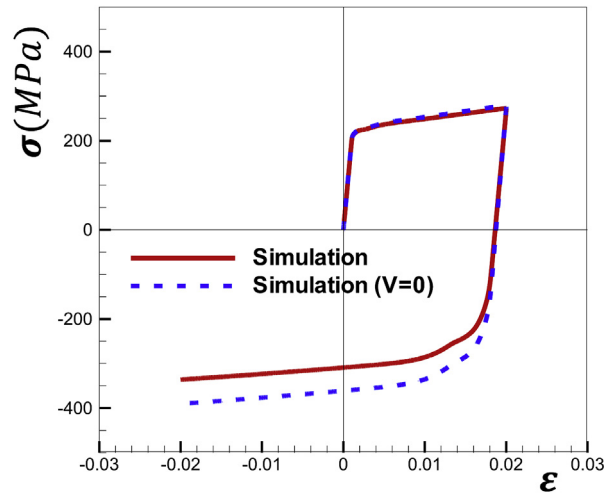
Fig. 9. Simulated tension-compression along the RD at 298 K and 1×10^{-4} s^{-1} for the 316L stainless steel used in this work. The simulation with $V = \text{var}(\tau^s) = 0$ (Eq. (24)) corresponds to assuming no distribution of RSS on the slip systems.

Second, the statistically enriched description whereby a distribution of stress is assigned to the material point allows us treating strain path changes, such as cyclic loading or Bauschinger effect. For the sake of illustration the model was applied to simulate the response of stainless steel under tension followed by compression (Fig. 9). The stress upon reverse loading is 300 MPa, while the yielding stress under the reverse compression is −150 MPa, much lower than the expected yielding stress of −300 MPa. The effect is induced by the fact that upon reversal the resolved shear stress distribution 'shifts to the left' (Fig. 1b), and the tail of the distribution reaches the opposite threshold stress before the mean does so, with the consequence that motion of some dislocation segments is activated earlier. In order to quantify the effect of stress distribution, the simulated result is compared to a simulation where no spread in resolved shear stress is considered ($var(\tau^s) = 0$ in Eq. (24)). The homogenization polycrystal model EVPSC does give a Bauschinger effect associated with intergranular stress, but the intragranular stress distribution contributes significantly to the Bauschinger effect. The simulated Bauschinger effect is of the same order as the experimental one reported by Wollmershauser et al. (2012) for a 317L stainless steel. Notice that the material and the testing conditions were not the same as in Wollmershauser, and that we have not tested our 316L under reversal conditions. The model predicts a Bauschinger effect without need to introduce explicitly an empirical back stress (Wollmershauser et al., 2012), although the latter is implicit in the assumption of the resolved shear distribution. In recent work of (Kitayama et al., 2013; Wen et al., 2015) also invoke the assumption of back stress, to which they add a mechanism of dislocation recombination attributed to a separate population of annihilating reversible dislocations. Such recombination is active during an extended strain interval following reversals, and should lead to a measurable diffraction peak narrowing during reversals. Recombination is not accounted for in the model presented here.

4. Conclusion

A crystal plasticity model incorporating transition state theory is developed for polycrystalline materials, where the concept of yield surface at $\tau = \tau_c$ used by traditional crystal plasticity models is replaced by the presence of a distribution of internal stress and thermal activation of dislocation de-pinning. The model is applied to study the mechanical behavior of stainless steel during different mechanical regimes. As the results of Section 3 demonstrate, the model explains several plastic deformation regimes with a single set of parameters, as follows:

1. The model accounts for the rate sensitivity of a material via its dependence on the dislocation activation energy. As a result, the model captures the right time dependence of stress decay and creep rate that take place during the stress and strain relaxation regimes, respectively.
2. The dependence on activation energy also allows accounting for temperature effect on the yield stress. A temperature increase will induce lower flow stress and higher hardening rate, which is consistent with the experimental observations.
3. The Bauschinger effect, which cannot be captured by traditional crystal plasticity models without additional assumptions, such as the empirical introduction of a back-stress as an extra term (Wollmershauser et al., 2012). In the current model the back stress is provided by the dispersion of RSS acting on each slip system.
4. In addition to the macroscopic behaviors mentioned above, the TST model also captures the crystallographic elastic strains and, most important, it connects the diffraction peak broadening with the stored dislocation density, and reproduces the observed peak widths (or standard deviations). The latter provides a direct connection between a model and measured peak profile.

Appendix A

Eq. (4) requires us to calculate the following integral

$$\int_{-\infty}^{-\tau_c} -p\left(\tau - \overline{\tau}\right)d\tau + \int_{\tau_c}^{\infty} p\left(\tau - \overline{\tau}\right)d\tau + \int_{-\tau_c}^{\tau_c} exp\left(-\frac{\Delta G_0}{kT}\left(1-\left(\frac{|\tau|}{\tau_c}\right)^p\right)^q\right)sgn(\tau)p(\tau-\overline{\tau})d\tau \tag{A1}$$

In Eq. (A1), the probabilistic distribution function (PDF) $p(\tau-\overline{\tau})$ is given by Eq. (8)

$$\int_{-\infty}^{-\tau_c} -p\left(\tau - \overline{\tau}\right)d\tau + \int_{\tau_c}^{\infty} p\left(\tau - \overline{\tau}\right)d\tau = \int_{-\infty}^{-\tau_c} -\frac{1}{\sqrt{2\pi}V}exp\left(-\frac{(\tau-\overline{\tau})^2}{2V^2}\right)d\tau + \int_{\tau_c}^{\infty} \frac{1}{\sqrt{2\pi}V}exp\left(-\frac{(\tau-\overline{\tau})^2}{2V^2}\right)d\tau$$

$$= -\frac{1}{2}\left(1+erf\left(\frac{-\tau_c-\overline{\tau}}{\sqrt{2}\,V}\right)\right)+\frac{1}{2}\left(1-erf\left(\frac{\tau_c-\overline{\tau}}{\sqrt{2}\,V}\right)\right) = -\frac{1}{2}\left(erf\left(\frac{-\tau_c-\overline{\tau}}{\sqrt{2}\,V}\right)+erf\left(\frac{\tau_c-\overline{\tau}}{\sqrt{2}\,V}\right)\right) \tag{A2}$$

$$\frac{d\overline{\dot{\gamma}}}{d\overline{\tau}} = c_v\rho b\left(p\left(-\tau_c-\overline{\tau}\right)+p\left(\tau_c-\overline{\tau}\right)+\int_{-\tau_c}^{\tau_c} exp\left(-\frac{\Delta G_0}{kT}\left(1-\left(\frac{|\tau|}{\tau_c}\right)^p\right)^q\right)dp\left(\frac{\tau-\overline{\tau})}{d\overline{\tau}\,d\tau}\right)\right) \tag{A3}$$

$$M^p_{ijkl} = \frac{\partial\dot{\varepsilon}^p_{ij}}{\partial\sigma_{kl}} = \sum_{s=1}^{N^{sys}}\frac{\overline{\dot{\gamma}^s}}{\partial\sigma_{kl}}m^s_{ij} = \sum_{s=1}^{N^{sys}}\frac{\overline{\dot{\gamma}^s}}{\partial\tau^s}m^s_{ij}m^s_{kl} \tag{A4}$$

The integrals $\int_{-\tau_c}^{\tau_c} exp\left(-\frac{\Delta G_0}{kT}\left(1-\left(\frac{|\tau|}{\tau_c}\right)^p\right)^q\right)sgn(\tau)p(\tau-\overline{\tau})d\tau$ and $\int_{-\tau_c}^{\tau_c} exp\left(-\frac{\Delta G_0}{kT}\left(1-\left(\frac{|\tau|}{\tau_c}\right)^p\right)^q\right)\frac{dp(\tau-\overline{\tau})}{d\overline{\tau}}d\tau$ are calculated using the Gauss Legendre quadrature method. Figure A1 shows the effect of the Gauss points considered on the predicted stress strain curves. Using 8, 16, or 32 Gauss points gives nearly the same stress strain curves. Therefore in this work, 16 Gauss points are selected for all simulations.
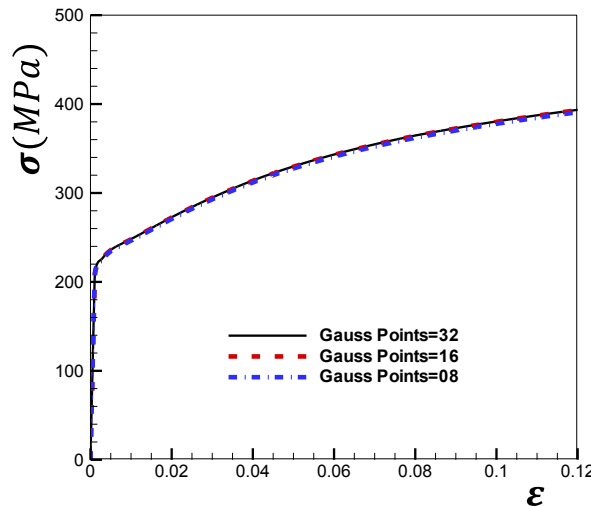

Fig. A1. Comparison of the stress strain curves obtained using various number of Gauss points.

Appendix B

Assume 'a' and 'b' are physical magnitudes, either function of position ($a(x)$, $b(x)$) or described by probability distribution functions $p_a(a)$ and $p_b(b)$. The average of 'a' over a material point is:

$$\bar{a} = \frac{1}{V} \int a(x)dV = \int_{-\infty}^{\infty} p(a)ada \tag{B1}$$

The variance of a is the second moment of the distribution and measures the spread of the variables. It is defined as:

$$var(a) = \frac{1}{V} \int (a - \bar{a})^2 dV = \int_{-\infty}^{\infty} p(a)(a - \bar{a})^2 da \tag{B2}$$

The standard deviation, equal to the square root of the variance is a more often used measure of spread: $SD(a) = \sqrt{var(a)}$. The covariance of a and b is:

$$covar(a,b) = \frac{1}{V} \int (a - \bar{a})\left(b - \bar{b}\right)dV = \int_{-\infty}^{\infty} \int_{-\infty}^{\infty} p_{a|b}(a|b)(a - \bar{a})\left(b - \bar{b}\right)dadb \tag{B3}$$

where $p_{a|b}(a|b)$ is the joint probability distribution of a and b. If a and b are independent or uncorrelated, then

$$p_{a|b}(a|b) = p_a(a)p_b(b) \tag{B4}$$

and their covariance (Eq. (B3)) becomes zero:

$$covar(a,b) = \int_{-\infty}^{\infty} p_a(a)(a - \bar{a})da \int_{-\infty}^{\infty} p_b(b)\left(b - \bar{b}\right)db = 0 \tag{B5}$$

From the above definitions it follows that:

$$\begin{aligned}
var(a) &= covar(a,a) \\
var(\alpha a) &= \alpha^2 var(a) \\
var(a + b) &= var(a) + var(b) + 2covar(a,b) \\
var(a + b + c) &= var(a) + var(b) + var(c) + 2covar(a,b) + 2covar(a,c) + 2covar(b,c)
\end{aligned} \tag{B6}$$

A further property to be used here refers to the variance of a function $f(a)$ of the statistical variable a. Using a first order Taylor expansion leads to:

$$var(f(a)) = \left(f'(\bar{a})\right)^2 var(a) \tag{B7}$$

In this work, the symmetric tensors are represented in a b-basis of symmetric orthonormal second order tensors $b_{ij}^{\lambda}(\lambda = 1,6)$ with the property $b_{ij}^{\lambda} = b_{ji}^{\lambda}$; $b_{ij}^{\lambda}b_{ij}^{\lambda'} = \delta^{\lambda\lambda'}$ ($i,j = 1,3; \lambda, \lambda' = 1,6$). When represented in this basis the elastic strain, the stress, and the elastic stiffness tensors adopt the form:

$$\varepsilon_{ij}^{el} = \varepsilon^{\lambda} b_{ij}^{\lambda} \text{ where } \varepsilon^{\lambda} = \varepsilon_{ij}^{el} b_{ij}^{\lambda} \tag{B8}$$

$$\sigma_{ij} = \sigma^{\lambda} b_{ij}^{\lambda} \text{ where } \sigma^{\lambda} = \sigma_{ij} b_{ij}^{\lambda} \tag{B9}$$

$$C_{ijkl} = C^{\lambda\lambda'} b_{ij}^{\lambda} b_{kl}^{\lambda'} \text{ where } C^{\lambda\lambda'} = C_{ijkl} b_{ij}^{\lambda} b_{kl}^{\lambda'} \tag{B10}$$

In the current work we use the following basis of orthonormal symmetric tensors $b^{(\lambda)}$:

$$b^{(1)} = \frac{1}{\sqrt{6}} \begin{bmatrix} 1 & 0 & 0 \\ 0 & 1 & 0 \\ 0 & 0 & -2 \end{bmatrix}, \quad b^{(2)} = \frac{1}{\sqrt{2}} \begin{bmatrix} 1 & 0 & 0 \\ 0 & -1 & 0 \\ 0 & 0 & 0 \end{bmatrix}, \quad b^{(3)} = \frac{1}{\sqrt{2}} \begin{bmatrix} 0 & 0 & 0 \\ 0 & 0 & 1 \\ 0 & 1 & 0 \end{bmatrix}, \quad b^{(4)} = \frac{1}{\sqrt{2}} \begin{bmatrix} 0 & 0 & 1 \\ 0 & 1 & 0 \\ 1 & 0 & 0 \end{bmatrix}, \quad b^{(5)}$$

$$= \frac{1}{\sqrt{2}} \begin{bmatrix} 0 & 1 & 0 \\ 1 & 0 & 0 \\ 0 & 0 & 0 \end{bmatrix}, \quad b^{(6)} = \frac{1}{\sqrt{3}} \begin{bmatrix} 1 & 0 & 0 \\ 0 & 1 & 0 \\ 0 & 0 & 1 \end{bmatrix} \qquad (B11)$$

References

Abdolvand, H., Daymond, M.R., 2012. Internal strain and texture development during twinning: comparing neutron diffraction measurements with crystal plasticity finite-element approaches. Acta Mater 60, 2240–2248.

An, K., Skorpenske, H.D., Stoica, A.D., Ma, D., Wang, X.L., Cakmak, E., 2011. First in situ lattice strains measurements under load at VULCAN. Metall. Mater. Trans. A 42, 95–99.

Balogh, L., Ribárik, G., Ungár, T., 2006. Stacking faults and twin boundaries in fcc crystals determined by x-ray diffraction profile analysis. J. Appl. Phys. 100, 023512.

Balogh, L., Capolungo, L., Tomé, C.N., 2012. On the measure of dislocation densities from diffraction line profiles: a comparison with discrete dislocation methods. Acta Mater. 60, 1467–1477.

Bertin, N., Capolungo, L., Beyerlein, I.J., 2014. Hybrid dislocation dynamics based strain hardening constitutive model. Int. J. Plast. 49, 114–144.

Beyerlein, I.J., Tomé, C.N., 2008. A dislocation-based constitutive law for pure Zr including temperature effects. Int. J. Plast. 24, 867–895.

Busso, E.P., 1990. Cyclic Deformation of Monocrystalline Nickel Aluminide and High Temperature Coatings. Ph.D thesis. MIT.

Cheong, K.S., Busso, E.P., Arsenlis, A., 2005. A study of microstructural length scale effects on the behavior of FCC polycrystals using strain gradient concepts. Int. J. Plast. 21, 1797–1814.

Clausen, B., Lorentzen, T., Bourke, M.A.M., Daymond, M.R., 1999. Lattice strain evolution during uniaxial tensile loading of stainless steel. Mater. Sci. Eng. A 259, 17–24.

Csikor, F.F., Groma, I., 2004. Probability distribution of internal stress in relaxed dislocation systems. Phys. Rev. B 70 article 064106.

Devincre, B., Hoc, T., Kubin, L., 2008. Dislocation mean free paths and strain hardening of crystals. Science 320, 1745–1748.

Drucker, D.C., Prager, W., 1952. Soil mechanics and plastic analysis or limit design. Q. Appl. Math. 10, 157–162.

Forest, S., 2009. Micromorphic approach for gradient elasticity, viscoplasticity, and damage. J. Eng. Mechanics-ASCE 135, 117–131.

Franciosi, P., Zaoui, A., 1982a. Multislip in fcc crystals a theoretical approach compared with experimental data. Acta Metall. 30, 1627–1637.

Franciosi, P., Zaoui, A., 1982b. Multislip tests on copper-crystals-a junctions hardening effect. Acta Metall. 30, 2141–2151.

Granato, A.V., Lücke, K., 1956. Theory of mechanical damping due to dislocations. J. Appl. Phys. 27, 583–593.

Granato, A.V., Hikata, A., Lucke, K., 1958. Recovery of damping and modulus changes following plastic deformation. Acta Metall. 6, 470–480.

Granato, A.V., Lücke, K., Schlipf, J., Teutonico, L.J., 1964. Entropy factors for thermally activated unpinning of dislocations. J. Appl. Phys. 35, 2732–2745.

Groma, I., Bakó, B., 1998. Probability distribution of internal stresses in parallel straight dislocation systems. Phys. Rev. B58, 2969–2974.

Groma, I., Ungar, T., Wilkens, M., 1988. Asymmetric x-ray-line broadening of plastically deformed-crystals .1. Theory. J. Appl. Crystallogr. 21, 47–53.

Groma, I., Csiker, F.F., Zaiser, M., 2003. Spatial correlations and higher-order gradient terms in a continuum description of dislocation dynamics. Acta Mater. 51, 1271–1281.

Guo, X.Q., Wu, P.D., Wang, H., Mao, X.B., 2015. Study of lattice strain evolution in stainless steel under tension: the role of self-consistent plasticity model. Steel Res. Int. 86, 894–901.

Gurtin, M.E., 2000. On the plasticity of single crystals: free energy, microforce, plastic-strain gradient. J. Mech. Phys. Solids 48, 989–1036.

Hirth, J.P., Lothe, J., 1982. Theory of Dislocations. Krieger Publishing Company.

Kanjarla, A.K., Lebensohn, R.A., Balogh, L., Tomé, C.N., 2012. Study of internal lattice strain distributions in stainless steel using a full-field elasto-viscoplastic formulation based on fast Fourier transformation. Acta Mater. 60, 3094–3106.

Karaman, I., Sehitoglu, H., Maier, H.J., Chumlyakov, Y.I., 2001. Competing mechanisms and modeling of deformation in austenitic stainless steel single crystals with and without nitrogen. Acta Mater. 49, 3919–3933.

Kitayama, K., Tomé, C.N., Rauch, E.F., Grácio, J.J., Barlat, F., 2013. A crystallographic dislocation model for describing hardening of polycrystals during strain path changes. Application to low carbon steels. Int. J. Plast. 46, 54–69.

Knezevic, M., Zecevic, M., Beyerlein, I.J., Bingert, J.F., McCabe, R.J., 2015. Strain rate and temperature effects on the selection of primary and secondary slip and twinning systems in HCP Zr. Acta Mater 88, 55–73.

Kocks, U.F., Argon, A.S., Ashby, M.F., 1975. Thermodynamics and kinetics of slip. Prog. Mater. Sci. 19, 1–281.

Kuhlmann-Wilsdorf, D., Wilsdorf, H., 1953. The surface structures of deformed aluminium, copper, silver, and alpha-brass, and their theoretical interpretation. Acta Metallurgica 394–413.

Larson, A.C., Von Dreele, R.B., 2004. GSAS Manual. Los Alamos National Laboratory. LAUR 86–748.

Lebensohn, R.A., Brenner, R., Castelnau, O., Rollett, A.D., 2008. Orientation image-based micromechanical modelling of subgrain texture evolution in polycrystalline copper. Acta Mater 56, 3914–3926.

Lee, S.Y., Wang, H., Gharghouri, M.A., Nayyeri, G., Woo, W., Shin, E., Wu, P.D., Poole, W.J., Wu, W., An, K., 2014. Deformation behavior of solid-solution-strengthened Mg–9 wt.% Al alloy: in situ neutron diffraction and elastic–viscoplastic self-consistent modeling. Acta Mater. 73, 139–148.

Li, L., Van Petegem, S., Van Swygenhoven, H., Anderson, P.M., 2012. Slip-induced intergranular stress redistribution in nanocrystalline Ni. Acta Mater. 60, 7001–7010.

Madec, R., Devincre, B., Kubin, L.P., 2002. From dislocation junctions to forest hardening. Phys. Rev. Lett. 89 article 255508.

McDowell, D.L., 1995. Stress state dependence of cyclic ratchetting behavior of two rail steels. Int. J. Plast. 11, 397–421.

McDowell, D.L., 2008. Viscoplasticity of heterogeneous metallic materials. Mater. Sci. Eng. R Rep. 62, 67–123.

Miller, M.P., Park, J.S., Dawson, P.R., Han, T.S., 2008. Measuring and modeling distributions of stress state in deforming polycrystals. Acta Mater 56, 3927–3939.

Monnet, G., Pouchon, M.A., 2013. Determination of the critical resolved shear stress and the friction stress in austenitic stainless steels by compression of pillars extracted from single grains. Mater. Lett. 98, 128–130.

Monnet, G., Devincre, B., Kubin, L.P., 2004. Dislocation study of prismatic slip systems and their interactions in hexagonal close packed metals: application to zeirconium. Acta Mater. 52, 4317–4328.

Monnet, G., Vincent, L., Devincre, B., 2013. Dislocation-dynamics based crystal plasticity law for the low- and high-temperature deformation regimes of bcc crystal. Acta Mater. 61, 6178–6190.

Picu, R.C., 2002. On the functional form of non-local elasticity kernels. J. Mech. Phys. Solids 50, 1923–1939.

Proust, G., Tomé, C.N., Jain, A., Agnew, S.R., 2009. Modeling the effect of twinning and detwinning during strain path changes of Mg alloy AZ31. Int. J. Plast. 25, 861–880.

Qiao, H., Wu, P.D., Wang, H., Gharghouri, M.A., Daymond, M.R., 2015. Evaluation of elastic–viscoplastic self-consistent polycrystal plasticity models for zirconium alloys. Int. J. Solids Struct. 71, 308–322.

Queyreau, S., Monnet, G., Devincre, B., 2009. Slip systems interactions in alpha-iron determined by dislocation dynamics simulations. Int. J. Plast. 25, 361–377.

Talyan, V., Wagoner, R.H., Lee, J.K., 1998. Formability of stainless steel. Metall. Mater. Trans. A 29, 2161–2172.

Ungár, T., Dragomir, I., Révész, Á., Borbély, A., 1999. The contrast factors of dislocations in cubic crystals: the dislocation model of strain anisotropy in practice. J. Appl. Crystallogr. 32, 992–1002.

Ungár, T., Gubicza, J., Ribárik, G., Borbély, A., 2001. Crystallite size distribution and dislocation structure determined by diffraction profile analysis: principles and practical application to cubic and hexagonal crystals. J. Appl. Crystallogr. 34, 298–310.

Ungár, T., Ribárik, G., Balogh, L., Salem, A.A., Semiatin, S.L., Vaughan, G.B.M., 2010. Burgers vector population, dislocation types and dislocation densities in single grains extracted from a polycrystalline commercial-purity Ti specimen by X-ray line-profile analysis. Scr. Mater. 63, 69–72.

Vineyard, G.H., 1957. Frequency factors and isotope effects in solid state rate processes. J. Phys. Chem. Solids 3, 121–127.

Voce, E., 1948. The relationship between stress and strain for homogeneous deformation. J. Inst. Metals 74, 537–562.

Wang, H., Wu, P.D., Tomé, C.N., Huang, Y., 2010a. A finite strain elastic–viscoplastic self-consistent model for polycrystalline materials. J. Mech. Phys. Solids 58, 594–612.

Wang, H., Raeisinia, B., Wu, P.D., Agnew, S.R., Tomé, C.N., 2010b. Evaluation of self-consistent polycrystal plasticity models for magnesium alloy AZ31B sheet. Int. J. Solids Struct. 47, 2905–2917.

Wang, H., Wu, P.D., Boyle, K.P., Neale, K.W., 2011. On crystal plasticity formability analysis for magnesium alloy sheets. Int. J. Solids Struct. 48, 1000–1010.

Wang, H., Wu, P.D., Tomé, C.N., Wang, J., 2012. Study of lattice strains in magnesium alloy AZ31 based on a large strain elastic-viscoplastic self-consistent polycrystal model. Int. J. Solids Struct. 49, 2155–2167.

Wang, H., Clausen, B., Tomé, C.N., Wu, P.D., 2013a. Studying the effect of stress relaxation and creep on lattice strain evolution of stainless steel under tension. Acta Mater 61, 1179–1188.

Wang, H., Wu, P.D., Wang, J., Tomé, C.N., 2013b. A crystal plasticity model for hexagonal close packed (HCP) crystals including twinning and de-twinning mechanisms. Int. J. Plast. 49, 36–52.

Wang, H., Wu, P.D., Wang, J., 2013c. Modeling inelastic behavior of magnesium alloys during cyclic loading–unloading. Int. J. Plast. 47, 49–64.

Wang, H., Wu, P.D., Lee, S.Y., Wang, J., Neale, K.W., 2015a. Numerical study of the effects of shear deformation and superimposed hydrostatic pressure on the formability of AZ31B sheet at room temperature. Int. J. Mech. Sci. 92, 70–79.

Wang, H., Wu, P.D., Wang, J., 2015b. Modelling the role of slips and twins in magnesium alloys under cyclic shear. Comput. Mater. Sci. 96, 214–218.

Wang, H., Clausen, B., Capolungo, L., Beyerlein, I.J., Wang, J., Tomé, C.N., 2016a. Stress and strain relaxation in magnesium AZ31 rolled plate: in-situ neutron measurement and elastic viscoplastic polycrystal modeling. Int. J. Plast. 79, 275–292.

Wang, H., Jeong, Y., Clausen, B., Liu, Y., Mccabe, R.J., Barlat, F., Tomé, C.N., 2016b. Effect of martensitic phase transformation on the behavior of 304 austenitic stainless steel under tension. Mater. Sci. Eng. A649, 174–183.

Warren, B.E., Averbach, B.L., 1950. J. Appl. Phys. 21, 595–599.

Wen, W., Borodachenkova, M., Tomé, C.N., Vincze, G., Rauch, E.F., Barlat, F., Grácio, J.J., 2015. Mechanical behavior of Mg subjected to strain path changes: experiments and modeling. Int. J. Plast. 73, 171–183.

Wenk, H.-R., Lutterotti, L., Vogel, S., 2003. Texture analysis with the new HIPPO TOF diffractometer. Nucl. Instrum. Methods Phys. 575–588. A515.

Wilkens, M., 1970. In: Simmons, J.A., de Wit, R., Bullough, R. (Eds.), Fundamental Aspects of Dislocation Theory, vol. II. Nat. Bur. Stand. (US) Spec. Publ. No. 317, Washington, DC, USA, p. 1195, 1970.

Wollmershauser, J.A., Clausen, B., Agnew, S.R., 2012. A slip system-based kinematic hardening model application to in situ neutron diffraction of cyclic deformation of austenitic stainless steel. Int. J. Fatigue 36, 181–193.

Wu, P.D., Wang, H., Neale, K.W., 2012. On the large strain torsion of HCP polycrystals. Int. J. Appl. Mech. 4, 1250024.